Dalton Transactions

Uranyl Uptake into Metal–Organic Frameworks: A Detailed X-Ray Structural Analysis

Journal:	*Dalton Transactions*
Manuscript ID	DT-ART-12-2023-004284.R1
Article Type:	Paper
Date Submitted by the Author:	09-Feb-2024
Complete List of Authors:	Heaney, Matthew; Washington State University, Chemistry Johnson, Hannah; Washington State University, Chemistry Knapp, Julia; Northwestern University, Chemistry Bang, Shinhyo; Washington State University, Chemistry Seifert, Sönke; Argonne National Laboratory, X-ray Science Division Yaw, Natalie; Washington State University, Chemistry Li, Jiahong; Washington State University College of Arts and Sciences, Chemistry Farha, Omar; Northwestern University, Chemistry Zhang, Qiang; Washington State University, Chemistry Moreau, Liane; Washington State University, Chemistry

ARTICLE

Uranyl Uptake into Metal–Organic Frameworks: A Detailed X-Ray Structural Analysis

Received 00th January 20xx,
Accepted 00th January 20xx

DOI: 10.1039/x0xx00000x

Matthew P. Heaney,[a] Hannah M. Johnson,[a] Julia G. Knapp,[b] Shinhyo Bang,[a] Soenke Seifert,[c] Natalie S. Yaw,[a] Jiahong Li,[a] Omar K. Farha,[b] Qiang Zhang,[a] and Liane M. Moreau*[a]

Metal-organic frameworks (MOF) are a subclass of porous framework materials that have been used for a wide variety of applications in sensing, catalysis, and remediation. Among these myriad applications is their remarkable ability to capture substances in a variety of environments ranging from benign to extreme. Among the most common and problematic substances found throughout the world's oceans and water supplies is $[UO_2]^{2+}$, a common mobile ion of uranium, which is found both naturally and as a result of anthropogenic activities, leading to problematic environmental contamination. While some MOFs possess high capability for the uptake of $[UO_2]^{2+}$, many more of the thousands of MOFs and their modifications that have been produced over the years have yet to be studied for their ability to uptake $[UO_2]^{2+}$. However, studying the thousands of MOFs and their modifications presents an incredibly difficult task. As such, a way to narrow down the numbers seems imperative. Herein, we evaluate the binding behaviors as well as identify the specific binding sites of $[UO_2]^{2+}$ incorporated into six different Zr MOFs to elucidate specific features that improve $[UO_2]^{2+}$ uptake. In doing so, we also present a method for the determination and verification of these binding sites by Anomalous wide-angle X-ray scattering, X-ray fluorescence, and X-ray absorption spectroscopy. This research not only presents a way for future research into the uptake of $[UO_2]^{2+}$ into MOFs to be conducted but also a means to evaluate MOFs more generally for the uptake of other compounds to be applied for environmental remediation and improvement of ecosystems globally.

Introduction

Uranyl, commonly written as $[UO_2]^{2+}$, is one of the most prominent forms of uranium found throughout environmental systems and the nuclear fuel cycle due to its stability under ambient conditions. [1-3] Although $[UO_2]^{2+}$ is present in many environmental systems at low concentrations naturally, at higher concentrations, it can pose a risk to local environments and those that depend upon them. Coupled with its toxicity and radioactivity is the long half-life of most common uranium isotopes, which extend into millions and billions of years, making the release of uranium a problem that cannot simply be solved by waiting for it to decay. As such, many efforts have been put forward in environmental remediation to sequester excessive amounts of $[UO_2]^{2+}$ released into the environment because of nuclear accidents. From the remediation of past accidents like the 2011 Fukushima Daiichi Nuclear Power Plant Disaster to response methods to potential future incidents involving leaks in spent nuclear fuel casks in interim and long-term storage, $[UO_2]^{2+}$ sequestration remains a primary focus for dealing with risky levels of uranium in the environment. [4-6]

Despite its chemical toxicity and radioactivity, uranium's necessity in nuclear energy production as a carbon-free, on-demand power source is often enough to balance potential hazards. Given the global movement to lower carbon emissions in the face of climate change and the lack of growth capacity for renewable energy sources such as wind and solar to replace non-renewables, a growing number of people, organizations, and governments are moving towards nuclear. This growing demand and necessity for uranium make it and its waste products in wastestreams an unavoidable concern. [7-9]

The increased interest in nuclear also poses additional problems, namely, how will future demand for uranium be met? As current sites become depleted, further exploration would be needed to find new sources as well as the harvesting of previously known but not economically viable sources. Several alternative sources have been proposed to meet this demand, all of which involve the production or use of $[UO_2]^{2+}$. One such method includes the extraction of $[UO_2]^{2+}$, which is naturally present in seawater. [10, 11] This is of particular interest as currently identified terrestrial resources are estimated to total 58.7 million tons of uranium (tU) whereas uranium present in the ocean is estimated to total 4-5 billion tU. However, the uranium present in seawater is at a concentration of 3-4 ppb, which is far lower than most terrestrial resources. [12] Therefore, novel methods of extraction would be needed to make use of seawater uranium resources.

[a] Department of Chemistry, Washington State University, Pullman, WA, 99164 USA. E-mail: liane.moreau@wsu.edu.
[b] Department of Chemistry, Northwestern University, 2145 Sheridan Road, Evanston, Illinois 60208-3113, USA.
[c] X-ray sciences Division, Argonne National Laboratory, Argonne, Illinois 60439, USA.

Electronic Supplementary Information (ESI) available: [details of any supplementary information available should be included here]. See DOI: 10.1039/x0xx00000x

A number of materials and methods have been proposed for the separation and sequestration of $[UO_2]^{2+}$ from a variety of sources, including seawater, but of particular interest are metal-organic frameworks (MOFs). One of the particularly beneficial features of MOFs for $[UO_2]^{2+}$ capture is their recyclability, as they show little drop in capacity for $[UO_2]^{2+}$ capture following repeated recycling. [13] Generally, MOFs are a class of materials consisting of a network of metal nodes connected by organic linker molecules to form highly porous, crystalline materials. The large number of nanoscale pores as well as high levels of tunability in MOFs allows for their long and diverse list of potential applications. MOFs have presented a rather broad and applicable means for catalysis, [14] sensing, [15] and capture of various compounds. [16-19] To date, several MOFs have been studied for their ability to uptake $[UO_2]^{2+}$.[19-23]

The ever-growing list of MOFs, as well as the various modifications that can be done to each, has risen into the tens of thousands, [24] which presents an impossibly large number of experiments to evaluate $[UO_2]^{2+}$ uptake to find the most effective ones. As such, it is imperative to shorten that list by looking at how certain characteristics of MOFs influence $[UO_2]^{2+}$ uptake and how $[UO_2]^{2+}$ is binding to better inform what MOFs would be best for capture. Unfortunately, to date there is a general lack of understanding of exactly where $[UO_2]^{2+}$ is binding within the MOFs. Comprehensive structural characterization of $[UO_2]^{2+}$ binding sites within MOFs is crucial to informing uptake mechanisms. This will require use of advanced structural characterization tools working in tandem to elucidate $[UO_2]^{2+}$- MOF bonding arrangements. We propose and demonstrate herein a method to combine two advanced X-ray characterization tools that are element-specific to interrogate uranium to achieve this aim. These include anomalous wide-angle X-ray scattering (AWAXS), which will provide the crystallographic planes within the MOF that contain uranium and extended X-ray absorption fine structure (EXAFS) spectroscopy, which will provide the local uranium binding structure within the MOF. Through this approach, we are able to propose binding sites for $[UO_2]^{2+}$ inside of Zr-based MOFs and make connections to trends in $[UO_2]^{2+}$ uptake. In addition to providing a method to assist in correlating structural trends with $[UO_2]^{2+}$ uptake, knowledge from this study and extended approach could be used to further potential applications of MOFs with incorporated $[UO_2]^{2+}$ such as forming UO_2 nanoparticles. [25-27]

In this work, we investigate a total of six different MOFs, all containing Zr_6 nodes, with different linker chemistries and pore structures to probe their different behaviors with regard to $[UO_2]^{2+}$ incorporation. Zr_6 nodes are a structure of 6 Zr atoms arranged in an octahedron, which are linked together by μ_3-O and μ_3-OH. The node itself, in a free state, is metastable but is stabilized by the presence of organic ligands. Which, in the case of MOFs, are the organic linkers. The Zr atoms of the node itself, without the presence of an organic linker directly bound to them, as is the case with a Zr_6 node with less than 12 coordinated linkers, will frequently bind what it can to achieve more stable coordination. [28, 29] It is for this reason that Zr_6 node containing MOFs often exhibit catalytic activity. [30, 31] However, the choice to specifically study Zr MOFs was also because they are generally highly stable, easy to make and modify, and present high crystallinity. Furthermore, all MOFs used were chosen based on their large pore size, high thermal stability, and broad pH stability, as these are all factors known to improve incorporation capacity and applicability to the systems where $[UO_2]^{2+}$ is found. [32, 33] Larger pores naturally would provide more space and locations for the binding of $[UO_2]^{2+}$ while stability to temperature and pH extremes allows for application in more extreme environments where $[UO_2]^{2+}$ might be found. [34] The MOFs UiO-67, NU-1000, PCN-224, and MOF-545 (also known as PCN-222) [35] were chosen for this work to investigate linker chemistry and structure effects as seen in Table 1.

Table 1 Pore properties investigated and probed by chosen MOFs

MOF	Pore Structure	Linker Chemistry	Pore Size (Å)
UiO-67	Cage	Hydrocarbon	10.9
UiO-66	Cage	Hydrocarbon	7.9
PCN-224	Cage	Porphyrin	22.5
NU-1000	Channel	Hydrocarbon	35.7
MOF-545	Channel	Porphyrin	39.2

The aforementioned four MOFs were also chosen based on previously published results showing additional desirable characteristics for $[UO_2]^{2+}$ sequestration systems, such as high resistance to gamma irradiation, high performance in the removal of other heavy metal ions, and selectivity. [36-38] Furthermore, MOFs similar to UiO-67 were also investigated using EXAFS to elucidate any effects in $[UO_2]^{2+}$ binding that might be caused by more minor linker differences. The two similar MOFs are listed in Table 2, along with their corresponding names and how their differences compare to UiO-67. It is worth noting that UiO-67/bpy is a mixed linker MOF which has partial substitution of the typical linker in UiO-67—biphenyl-4,4'-dicarboxylic acid (bpdc), for another linker—2,2'-bipyridine-5,5'-dicarboxylic acid (bpydc).

Table 2 Structures similar to UiO-67

	UiO-67	UiO-66	UiO-67/bpy
Linker	bpdc	Benzene-1,4-dicarboxylic acid	bpydc (25%) + bpdc (75%)
Comparison		Smaller pore size, similar aromatic linker chemistry	Similar pore size, nitrogen in linker could act as binding sites

Herein, we use a combination of X-ray fluorescence (XRF), X-ray absorption spectroscopy (XAS), which encompasses both EXAFS and X-ray absorption near edge structure (XANES), and AWAXS to investigate the binding behaviors of $[UO_2]^{2+}$ incorporated into chosen MOFs. The usage of XRF provides a means to quantify the uptake of U with respect to the Zr that make up the nodes of the MOFs and can be used to provide insight as to whether the number of proposed occupied sites from other techniques fits with the amount of U present. XAS provides a means to look at both the local environment

surrounding $[UO_2]^{2+}$ when bound in the MOF and the electronic state of U via EXAFS and XANES, respectively. Therefore, allowing for investigation of $[UO_2]^{2+}$ location and, by extension, its binding site, as well as the effects binding has on the electronic structure of the $[UO_2]^{2+}$. Lastly, AWAXS provides a selective method to find the crystallographic planes where U is present through the variation of incident X-ray energy and its effect on the diffraction intensity of planes. These three techniques combined allow for the determination of $[UO_2]^{2+}$ binding sites and the features that make an ideal MOF for $[UO_2]^{2+}$ capture.

Experimental

Caution

Natural uranium (^{nat}U) isotopes are α-emitting radioisotopes and present a radiological hazard as well as a heavy metal hazard. All handling of ^{nat}U materials were conducted under standard radioactive materials handling procedures. All experimental work involving ^{nat}U materials were conducted in a designated radiological lab inside fume hoods.

Synthesis

Previously published syntheses were followed to obtain UiO-66, [39] UiO-67, [39] NU-1000, [40] PCN-224, [41] and MOF-545. [41] The synthesis of UiO-67/bpy was performed by following the previously published synthesis of UiO-67. However, the 90 mg of linker used was a mixture of bpydc and bpdc at a composition of 25% bpydc and 75% bpdc, as opposed to the purely bpdc linker synthesis published previously. [39] This change is due to research indicating that the pure bpydc linker version of the MOF has reduced chemical stability. [42] It is worth noting that the synthetic procedure used for PCN-224 was reported as MOF-525. However, further research has shown that the original synthetic procedure for MOF-525 yields PCN-224. [43] Microscopy images and adsorption isotherms of selected MOFs are shown in Figures S1-S3 in the Supporting Information (ESI).

Solution-Phase Loading of $[UO_2]^{2+}$

Solutions of $[UO_2]^{2+}$ were prepared by dissolving $UO_2(NO_3)_2{\cdot}xH_2O$ (25 mg) in wet THF (5 mL). Before $[UO_2]^{2+}$ loading, MOFs (50 mg) were washed with acetone (40mL) three times using a centrifuge, followed by washing with THF (40mL) three times and was soaked in THF overnight on a vibratory shaker for solvent exchange. Following this, the MOFs were separated by centrifugation and decantation of THF. The previously made $UO_2(NO_3)_2$ THF solution was then added to the activated MOF powder to begin $[UO_2]^{2+}$ incorporation and was left on a vibratory shaker overnight. $[UO_2]^{2+}$ loaded MOFs were then separated by centrifugation, decantation of THF solution, immersed in fresh THF (40 mL), and left on a shaker overnight before being centrifuged and decanted to remove excess $[UO_2]^{2+}$. The washed MOFs were transferred to glass vials using THF. Solvent was removed by heating the vials in a sand bath at 80°C and leaving them under vacuum overnight. The resulting loaded MOFs were then sealed and used for characterization.

XRF

XRF data was collected on a Bruker Nano S2 Picofox XRF spectrometer equipped with a Mo X-ray source. Samples were prepared by taking dry MOFs and adhering them to a quartz disc with silicone grease. Amounts of U in each sample were determined by the relative ratios of the U Lα peak area to the Zr Kα peak area and applying appropriate corrections.

XAS

XAS data was collected in transmission mode at the U L_3 edge at Beamline 13-ID-E at the Advanced Photon Source with a beam size of 50 x 50 µm. Edge energies were calibrated to a Y foil. All samples were prepared by taking dried MOFs and mixing them with dry boron nitride (BN) to obtain optimal sample thickness. Samples were contained in an aluminum holder with indium seals and Kapton windows. The samples were moved every 3 scans in a raster and tested for beam damage. Data reduction and analysis were performed using the IFEFFIT software package. [44]

For extended X-ray absorption fine structure (EXAFS) data, the data was Fourier transformed in k-space and fit in R-space using the multiple k-weight fitting feature to relevant theoretical pathways generated by FEFF6. [45] The number of variables varied in the fit were limited to be less than two thirds the number of independent points and the fit was varied to achieve minimization of χ^2. For all MOF fits, only one average core atom site could be interrogated as calculating multiple core atom sites would result in a prohibitive number of pathways to adhere to the Nyquist criterion, therefore an average site was instead considered. Details of the fitting procedures can be found in the ESI.

AWAXS

AWAXS data was collected at Beamline 12-ID-C at the Advanced Photon Source on a SAXS pinhole setup with a sample to detector distance of 2.2 m. The data acquisition was done on a Dectris Pilatus 2M detector. Measurement energies were taken below and approaching the U L_3 absorption edge to observe anomalous behavior. Samples were prepared by mixing dried MOFs with dry BN and packed into 1.5 mm quartz capillaries. Capillaries were packed into Kapton tubes and sealed with epoxy before being placed into an aluminum holder with Kapton windows. Measurement data was reduced in Nika[46], processed in Irena[47] and packages for Igor Pro. Assignment of Miller indices were performed using GSAS-II[48] with previously published crystallographic information files (CIFs) of MOFs for unit cell parameters. [40, 41, 49, 50] A more detailed explanation of the analysis of AWAXS data can be found in the ESI.

Results and Discussion

XRF Results

XRF measurements are intended to confirm $[UO_2]^{2+}$ uptake into the MOFs. Specifically, in this work it is quantified relative to Zr as this provides information on the number of $[UO_2]^{2+}$ ions bound in an average unit cell of the loaded MOF. XRF data (Figure 1), was normalized to the Zr K_α peak to better show the differences in $[UO_2]^{2+}$ uptake compared with the amount of Zr present in each MOF. Integration results of the U L_α and Zr K_α peaks are shown in Table 3 as both relative ratios of U/Zr and percent relative abundances, with errors given to 1 standard deviation.

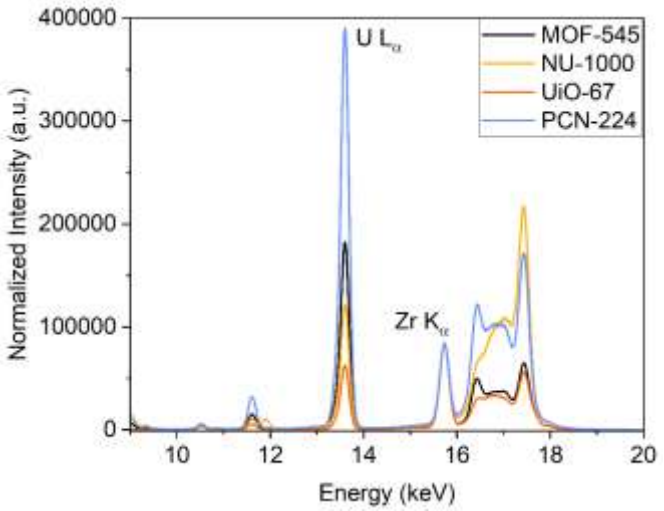

Figure 1 XRF spectra of selected MOFs normalized to Zr K_α peak. Figure shows increasing $[UO_2]^{2+}$ uptake from lowest to highest UiO-67<NU-1000<MOF-545<PCN-224.

Table 3 Relative ratios and percent abundance of U and Zr in selected MOFs from XRF.

		UiO-67	NU-1000	MOF-545	PCN-224
Relative Ratio (U/Zr)		0.63±0.01	0.79±0.02	1.858±0.009	3.98±0.01
Percent Relative Abundance	U	38±2%	56±2%	65±3%	80±2%
	Zr	61±2%	44±2%	35±3%	20±2%

AWAXS Results

Since AWAXS is a rare synchrotron based technique, and unfamiliar to most scientists an explanation of the technique is warranted. In its simplest form, AWAXS is a specialized type of wide-angle X-ray scattering (WAXS), which itself gives the same information as X-ray diffraction (XRD) – crystallographic planes, which is a much more familiar technique to most. So, for the sake of simplicity, one may consider WAXS no different than XRD. The "anomalous" part of AWAXS is an abbreviated wording for a variable energy technique in the X-ray science community. Therefore, one may consider AWAXS as a variable energy form of XRD.

The benefit that being able to vary energy in AWAXS comes from the competitive effect between scattering and absorption. In short, if scattering dominates, then absorption is minimized; conversely, if absorption dominates, then scattering is minimized. For all the elements, there are unique energies where the absorption of X-rays increases, frequently referred to as absorption edges, and the energies of these absorption edges do not precisely overlap with other elements. This provides an element-specific effect that can be exploited.

By varying the energy of incident X-rays in AWAXS it is possible to see which scattering (diffraction) peaks have specific elements contributing to the peak. For example, if the incidient X-ray energy is that of the absorption edge for a given element, then the amount that the element scatters (diffracts) is minimal reducing the intensity of specific scattering peaks that are contributed to by that element. Therefore, since scattering peaks are related to specific crystallographic planes one can identify which planes contain an element, or elements, of interest. In this way, AWAXS provides data on the specific

planes containing $[UO_2]^{2+}$, and by extension the specific binding sites as measurements were taken at energies well below and close to the U L_3 absorption edge. All AWAXS patterns of the various MOFs can be seen in Figures S4-S8 in the ESI. All assigned peaks with associated crystallographic planes exhibiting anomalous behavior are shown in Table 4. All planes with anomalous behavior can be expected to have $[UO_2]^{2+}$ present in the plane given the competitive effect between scattering and absorption as the energy of the incident beam approaches the U L_3 absorption edge. This leads to variations in scattering intensity. Furthermore, planes that become absent with loading and systematic absences that are present with loading are expected to have either $[UO_2]^{2+}$ or have some part of the structure along that plane distorted by $[UO_2]^{2+}$ binding, and are also given in Table 4, as there is a clear disruption in the pristine structure factor due to a change in the scatterer(s) present in that plane. In the case of a new absence, this

Table 4 Crystallographic planes exhibiting notable behaviors for selected MOFs with loading

MOF	Space Group (Number)	Crystallographic plane with anomalous behavior	Plane absent with loading	Systematic absence present with loading
NU-1000	P6/mmm (191)	(001), (110), (111), (201), (300), (211)	None	None
PCN-224	Im-3m (229)	(211), (220), (400)	(110), (411)/(310), (611)/(532)	(144)
MOF-545	P6/mmm (191)	(100), (001), (200), (201), (112), (300), (311), (400), (411)	None	None
UiO-67	Fm-3m (225)	None	None	None
UiO-67/bpy	Fm-3m (225)	None	None	None

indicates a regular binding of $[UO_2]^{2+}$ in that plane or distortion of the structure caused by the binding since it must be able to regularly disrupt the structure factor to remove the peak entirely. Alternatively, emergence of a systematic absence does not indicate regular binding or resulting distortion on that plane but rather enough binding or resulting distortion to make the diffraction observable. There are also instances of unique peaks that are not present in the pristine structure nor assignable to any particular crystallographic plane. These include the shoulder peak present in MOF-545 just below the (200) peak, and the shoulder peaks in PCN-224 just below the (310) peak and above the (211) peak, as well as a unique peak just above the (420) peak in PCN-224. It is expected that all these new peaks are due to a long-range ordering of $[UO_2]^{2+}$ present within the site, and are close to a neighboring plane in the pattern. It is also worth noting the (331) peak in UiO-67 and UiO-67/bpy is absent in the loaded pattern but only observable at higher energies and it is therefore not possible to establish if this peak has anomalous behavior, which appears absent near the absorption edge due to reduced scattering or if this is in fact a new systematic absence with loading.

XANES Results

Much like AWAXS, XANES is also an element-specific technique that results from the absorption of incident X-rays at and around the absorption edge of the element of interest. The amount of absorption at a given energy is affected by the electronic structure of the element itself, which may be due to a number of factors, such as the oxidation state, any charge transfer, and orbital mixing. This makes XANES a useful technique to probe the chemical fingerprint of materials and the direct electronic structure of an element in a material. Of particular interest is the oxidation state of the bound U in case some reduction occurs in binding to one of the studied MOFs. The XANES spectra, shown in Figure 2, of the loaded MOFs as well as UO_2 to act as a reference for a U(IV) oxidation state are given in normalized μ to better compare the electronic structure difference of U in each MOF. All bound U possesses a shoulder peak feature (~17183 eV) which occurs just above the maximum absorption, known as the "white line," in energy. While the intensity of the shoulder peak varies for each sample, the feature is reduced in intensity and more closely resembles the UO_2 standard, particularly for UiO-66, UiO-67 and UiO-67/bpy. This suggests that U is in a more reduced state from the initial U(VI). However, it is also pertinent to note that coordination geometry around U can affect this feature and makes definitive determination of the oxidation state difficult.

EXAFS Results

Like AWAXS and XANES, EXAFS is an element-specific technique, which is actually a continuation of absorption data from XANES into higher energies beyond those around the absorption edge of an element. The particular features that are used in EXAFS are due to modulations of absorption, which arise from the photoelectron that is ejected when an atom of the particular element absorbs an X-ray photon. This ejected photoelectron

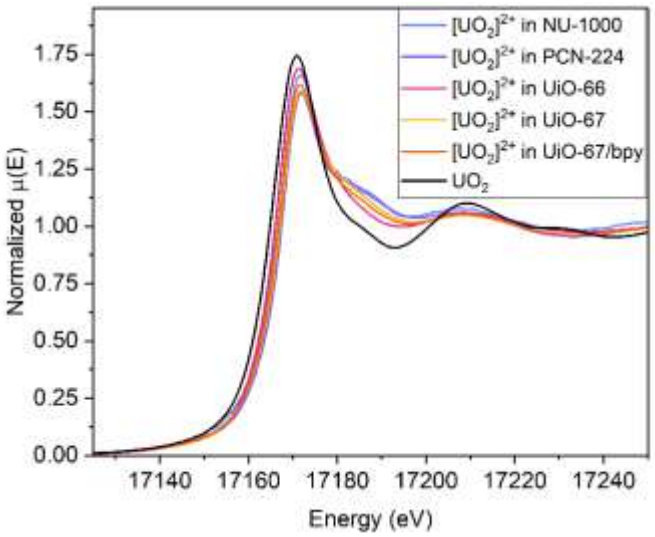

Figure 2 Combined XANES spectra of loaded MOFs and UO_2. Combined spectra show the differences in the electronic structure of U when bound in MOFs.

goes on to interact with the atoms of the surrounding environment as though it were a wave, due to the wave-particle duality of electrons, with the surrounding atoms scattering the wave. As a result of this scattering, constructive and destructive interference can occur and appear in EXAFS spectra in the form of modulations. These modulations can, in turn, provide specific information on the distance of the scattering atom from the atom that ejected the photoelectron, as well as information on the identity of the scattering atom. Combined, this information on distance and atom identity can be used to elucidate the local coordination environment around atoms of the specific element of interest. For this reason, EXAFS is used to provide information on the local environment around the bound $[UO_2]^{2+}$, which can be used to elucidate and evaluate the proposed binding site. The EXAFS spectra in R-space are shown in Figure 3 and fits and results are shown in Figures S9-S22 in the ESI. EXAFS spectra for UO_2 and $UO_2(NO_3)_2$ are also shown and fitted as references to the coordination environments of U(IV) and U(VI). Differing binding behaviors of $[UO_2]^{2+}$ are present between the MOFs as well as a deviation from the

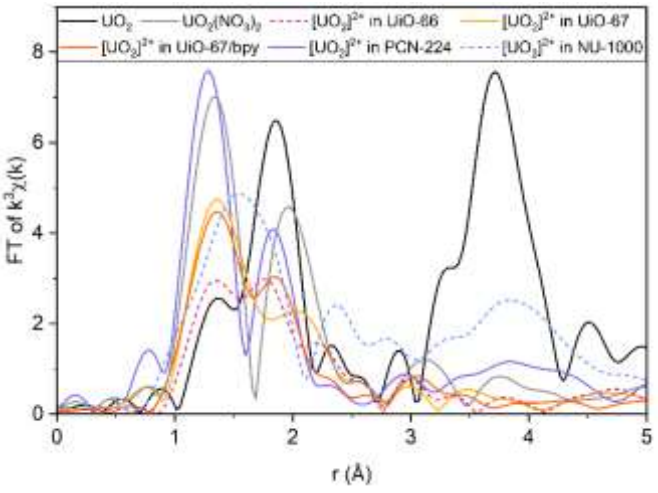

Figure 3 Combined R-space EXAFS spectra of loaded MOFs, UO_2, and $UO_2(NO_3)_2$. Combined spectra show the differences in electron density of different shells as a function of distance from the core U atom.

behavior of UO_2 and $UO_2(NO_3)_2$. These differences are most notably seen in the form of varied higher order shell intensities and different axial and equatorial contributions in the lower order shells. Additionally, given that only one core atom site can be investigated when fitting the MOFs, due to the number of pathways that would otherwise be generated from attempting to fit multiple sites likely violating the Nyquist criteria, fits act as an average of all sites that might be present. Therefore, the presence of multiple notably different sites could lead to greater error and/or higher mean squared disorder (σ^2)—the regularity of a peak appearing in a certain position, in fits.

Effects of Pore Structure and Type

The XRF results show the effect of pore structure and chemistry on uptake efficiency of $[UO_2]^{2+}$ into MOFs which contain either a cage (UiO-67 and PCN-224) or channel (NU-1000 and MOF-545) pore. In particular, the aim is to investigate whether the cage vs. channel structure may play a role depending on the identity of the linker. Furthermore, the coordination environment also plays a role in this as the Zr_6 node for UiO-67, as well as UiO-66 and UiO-67/bpy, is fully saturated, being coordinated to 12 linkers, while NU-1000 and MOF-545 are 8-coordinate, and PCN-224 is 6-coordinate. This difference in linker coordination on the Zr_6 node appears to increase uptake with decreasing coordination as with fewer linkers coordinated to the Zr_6 node there are more exposed O's and OH's that are bonded to the Zr in the node that can readily bind $[UO_2]^{2+}$. This could be linked to the observation that hydrocarbon cage pores uptake less than hydrocarbon channel pores while porphyrin channel pores will uptake less than porphyrin cage pores. However, additional MOF structures should be investigated to determine the universality of this trend. Alternatively, a clear connection can be drawn between the uptake efficiency and pore chemistry, with hydrocarbon pores (UiO-67 and NU-1000) having significantly lower uptake efficiency of $[UO_2]^{2+}$ than MOFs with porphyrin pores (MOF-545 and PCN-224) suggesting that there may be some evidence of $[UO_2]^{2+}$ binding to porphyrin sites on the linker, in addition to binding to the Zr_6 node, that leads to greater uptake efficiency. These results are corroborated by the AWAXS and XAS data.

Binding of $[UO_2]^{2+}$ to PCN-224

PCN-224 likely possesses two different types of binding sites, one on the Zr_6 node and the other on the porphyrin site. The AWAXS data of PCN-224 show anomalous behavior on the (110) and (411)/(310) planes which all exclusively intersect the Zr_6 node. However, all planes that exhibit anomalous behavior and intersect the porphyrin site also intersect the Zr_6 node, making it impossible to specifically attribute the anomalous behavior to $[UO_2]^{2+}$ in a porphyrin site. Additionally, the (200) peak, which does intersect the porphyrin sites exclusively, possesses behavior which cannot be defined as anomalous with certainty, as defined in the AWAXS analysis details in the ESI. Despite this lack of definitive evidence, the EXAFS data of PCN-224 suggests the presence of a second binding site as the large σ^2 in U-O shells beyond the first shell, are likely due to a second binding site. The reasoning for this is that O and N are indistinguishable in EXAFS analysis due to the similarity in their atomic number, and therefore atomic scattering factor. Therefore, fitting for U-O shells beyond the first shell could, in fact, be fitting U-N shells as well, leading to a high σ^2 to obtain a good fit due to the notable differences in the local environment between the Zr_6 node and porphyrin site. Furthermore, a means by which to obtain an 80±2% relative abundance of U to Zr can be obtained by having $[UO_2]^{2+}$ bound to both sides of the porphyrin site and to all six sites on the Zr_6 node like the proposed structure shown in Figure 4 in comparison to the unloaded sites shown as well.

The coordination of the U-O shells beyond the first would be fulfilled in both sites due to the presence of NO_3^{2-} and/or H_2O coordinating with the $[UO_2]^{2+}$ while it is bound to the sites and would further preserve the $[UO_2]^{2+}$ coordination environment like that seen in $UO_2(NO_3)_2$. This coordination would be expected to maintain the charge balance for U(VI) as is shown in Figure 2 of the XANES data of PCN-224 clearly exhibiting a shoulder and white line typical for $[UO_2]^{2+}$.

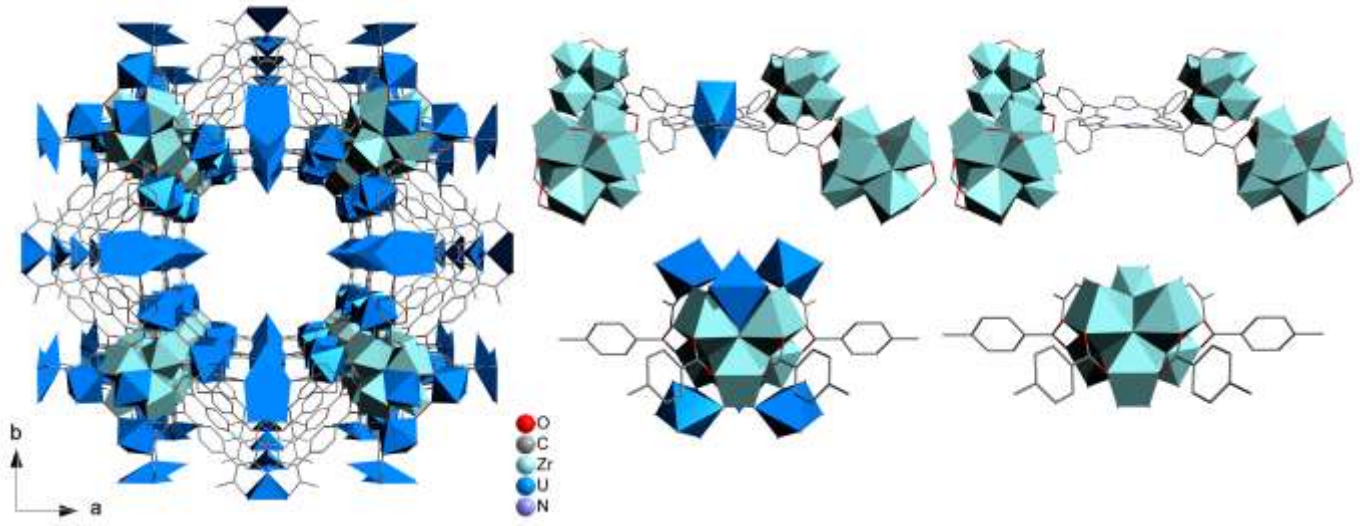

Figure 4 Proposed structure of PCN-224 with bound $[UO_2]^{2+}$ as well as focused images of proposed binding sites on the porphyrin and Zr_6 node in both their unloaded and loaded forms. Image is intended to show the two different types of binding sites and the overall appearance of a pore of PCN-224 when $[UO_2]^{2+}$ is bound.

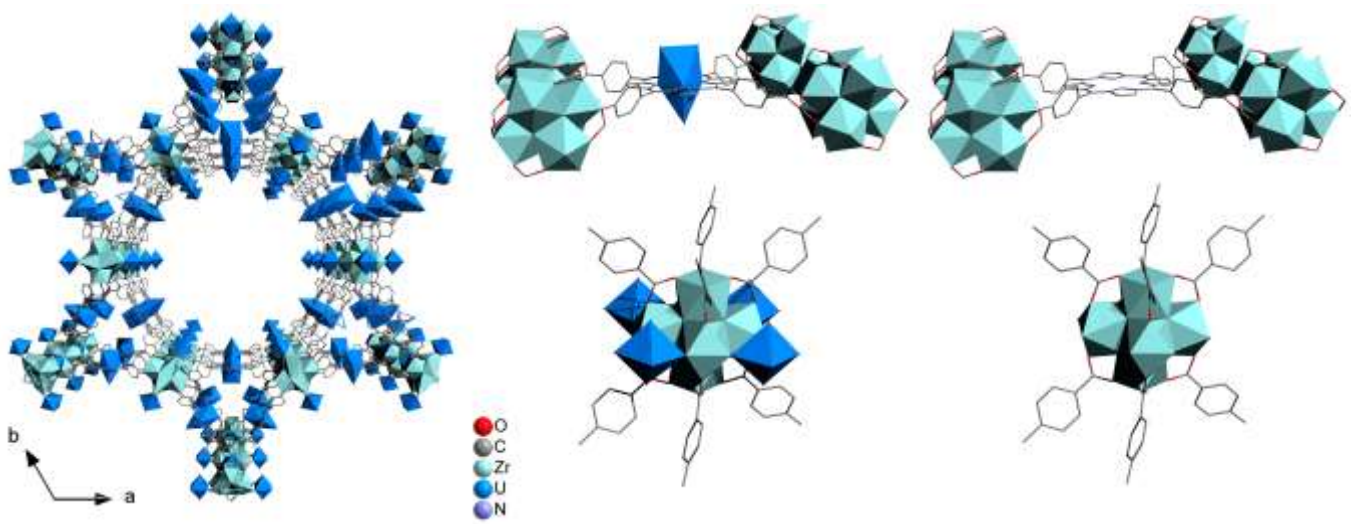

Figure 5 Proposed structure of MOF-545 with bound $[UO_2]^{2+}$ as well as focused images of proposed binding sites on the porphyrin and Zr_6 node in both their unloaded and loaded forms. Image is intended to show the two different types of binding sites and the overall appearance of a pore of MOF-545 when $[UO_2]^{2+}$ is bound.

Binding of $[UO_2]^{2+}$ to MOF-545

Like the results of PCN-224 there are also likely two binding sites at the Zr_6 node and the porphyrin for MOF-545. From the AWAXS data of MOF-545 the (100), (311), (411), and (300) planes all exclusively intersect sites on the Zr_6 node and exhibit anomalous behavior. Additionally, the (001), (201), and (400) planes, which exclusively intersect sites on the porphyrin, exhibit anomalous behavior. Therefore, suggesting the presence of $[UO_2]^{2+}$ in sites both on the porphyrin and the Zr_6 node. Coupled with the similarity in pore chemistry and high uptake of $[UO_2]^{2+}$, this brings further credence to $[UO_2]^{2+}$ binding to the porphyrin sites of both PCN-224 and MOF-545. Although, the lower uptake of $[UO_2]^{2+}$ by MOF-545 when compared to PCN-224 can be attributed to the lower amount of possible binding sites on the Zr_6 node as shown in Figure 5 in comparison to the unloaded sites shown as well. Furthermore, given the notable similarities between MOF-545 and PCN-224 it may be likely that the EXAFS and XANES spectra would exhibit similar features. However, further study would need to be conducted to test this as there exists the possibility of different charge balancing on the Zr_6 node due to the lower local concentration of $[UO_2]^{2+}$, which may affect XANES spectra and the distances obtained from EXAFS analysis.

Binding of $[UO_2]^{2+}$ to NU-1000

In the case of NU-1000 the uptake of $[UO_2]^{2+}$ could be achieved solely by binding to the Zr_6 node. However, contrary to previously published literature, which studied a single crystal of NU-1000, and therefore may not have been representative overall of the bulk MOF structure in all cases, [51] both EXAFS fitting, shown in Figure S11, and the AWAXS analysis indicate a strong likelihood of two sites that $[UO_2]^{2+}$ can bind to NU-1000 as shown in Figure 6, rather than a single site. In the case of the AWAXS results, the (111) and (211) planes, both of which behave anomalously, exclusively intersect the O binding sites that points along the linker plane, while the (001) and (110) planes, which also have anomalous behavior, exclusively intersect the O binding sites that point into the pores. In the EXAFS fitting there is more axial O coordination given by the first shell than typical $[UO_2]^{2+}$. However, the relatively close distance between U-Zr as well as the generally more prominent Zr and O shells than other samples suggest a higher interaction. Combined these factors suggest that $[UO_2]^{2+}$ is rather closely packed into its binding sites, which explains the higher O coordination. Furthermore, the higher σ^2 of both the first U-O shell and the U-Zr shell, corroborates finding of two different binding sites with similar character in O structure beyond the first shell. Attempts were made to test both sites specifically by fitting the U to only the parameters of one site. However, these fits resulted in nonphysical values (e.g., negative coordination numbers and disorder), further corroborating the existence of two binding sites. Given the uptake of $[UO_2]^{2+}$ observed for NU-1000 and the close packing of $[UO_2]^{2+}$ into binding sites on the Zr_6 node it seems likely that the sites may bind $[UO_2]^{2+}$ in either of the two ways shown in Figure 6, but not at the same time on the same node, as this would likely cause significant repulsion, which would not only contradict the close packing of $[UO_2]^{2+}$ in the binding sites on the Zr_6 node, but would also likely have a notable effect on the electronic structure of the U, which would be observed in XANES spectra. However, no notable deviation is observed between the XANES spectra of NU-1000 and the other MOFs that were studied.

Binding of $[UO_2]^{2+}$ to UiO-67

Like the XRF results of NU-1000, the uptake efficiency for UiO-67 could be achieved through solely binding to sites on the Zr_6 node. It is assumed that a similar uptake efficiency would be achieved for UiO-66 and UiO-67/bpy given both the similar results between these three and their similar structures. The lack of any definitively unique peaks, changes in systematic absences, or peaks with anomalous behavior in UiO-67 and UiO-67/bpy suggests a random binding within the MOF with no particular systematic orientation of the $[UO_2]^{2+}$ in the sites it binds to. However, in the AWAXS data, the cause of the (331)

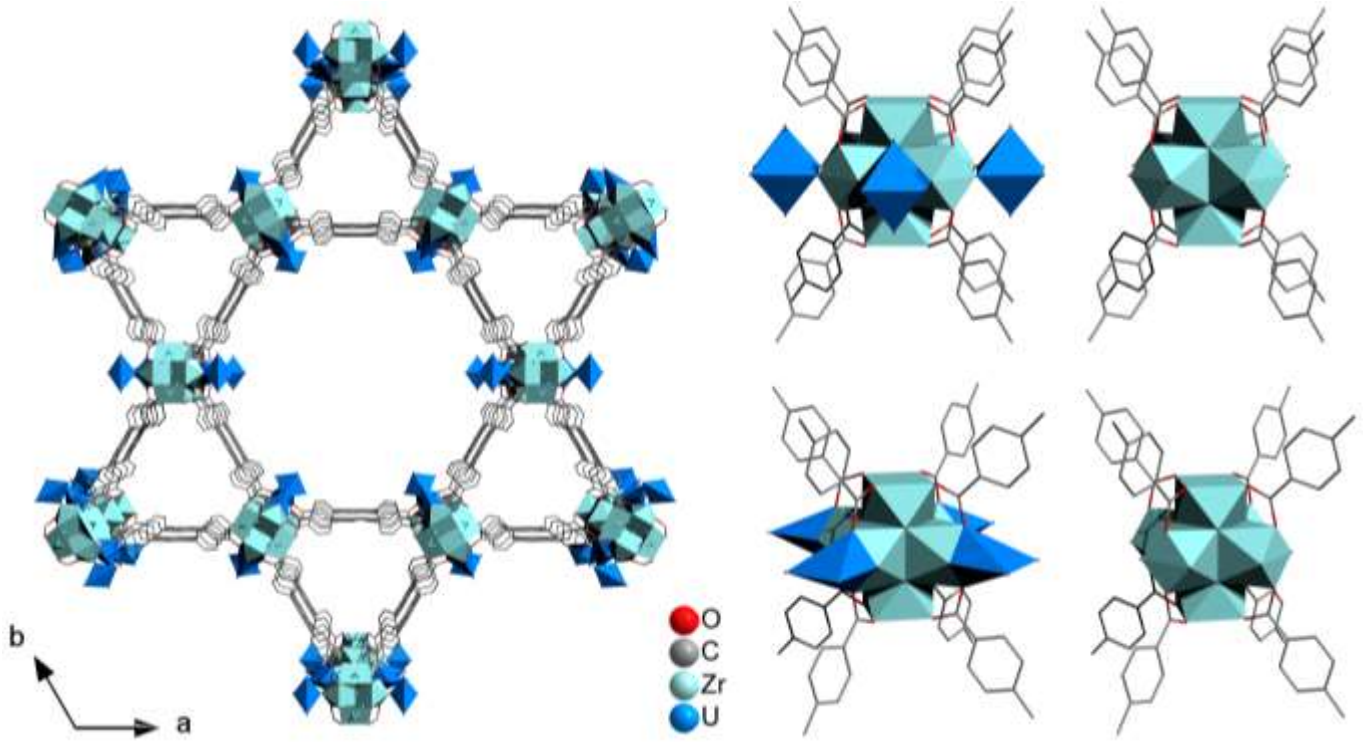

Figure 6 Proposed structure of NU-1000 with bound $[UO_2]^{2+}$ as well as focused images of proposed binding sites on the Zr_6 node in both their unloaded and loaded forms. Image is intended to show the two different ways $[UO_2]^{2+}$ binds to the Zr_6 node and the overall appearance of a pore of NU-1000 when $[UO_2]^{2+}$ is bound.

plane being absent with loading as either being caused by anomalous behavior that completely suppresses the peak near the absorption edge or a new systematic absence due to loading is not of importance as both indicate the presence of $[UO_2]^{2+}$ or a distortion in the structure caused by its binding to a site on the plane. However, this plane is of importance as it is the only plane present in the patterns which intersects the Zr_6 node, does not lie directly along the linkers, and intersects a site between the carboxylic acid groups of the linkers. This suggests that the $[UO_2]^{2+}$ might solely bind between carboxylic acid groups of the linker for UiO-67 near the Zr_6 node as shown in Figure 7 in comparison to the unloaded sites shown as well.

A similar structure is expected for UiO-67/bpy given similarity in linker and little difference between UiO-67 and UiO-67/bpy in their EXAFS fitting and XANES spectra. It is also notable that all the σ^2 values for UiO-67/bpy are higher than UiO-67, this can be either attributed to the sample having two structures present from a mixed linker composition between bpydc and bpdc or sites becoming more distorted when bpydc is the linker. Regarding the UiO-66 EXAFS fitting, there is a deviation from that of UiO-67 and UiO-67/bpy, most notably in the coordination of the first U-O shell. The lower coordination of UiO-66 compared to UiO-67 and UiO-67/bpy may be in part due to a charge compensation effect induced by the surrounding MOF structure that can be seen in the XANES data as UiO-66 possesses a notably lower $[UO_2]^{2+}$ shoulder from a less U(VI) character. While fitting for subsequent U-O shells in UiO-66 did not vary much between the three MOFs, with the exception of the fifth shell, this can be attributed to variable coordination of H_2O and NO_3^{2-}. However, the variation in the

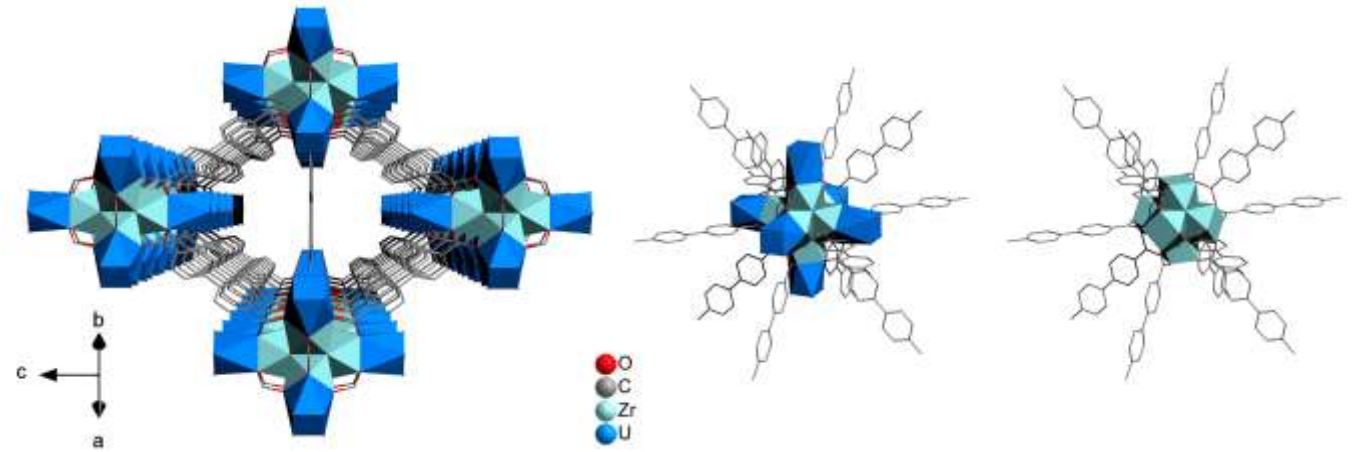

Figure 7 Proposed structure of UiO-67 with bound $[UO_2]^{2+}$ as well as a focused image of proposed binding sites on the Zr_6 node in both their unloaded and loaded forms. Image is intended to show the way $[UO_2]^{2+}$ binds to the Zr_6 node and the overall appearance of a pore of UiO-67 when $[UO_2]^{2+}$ is bound.

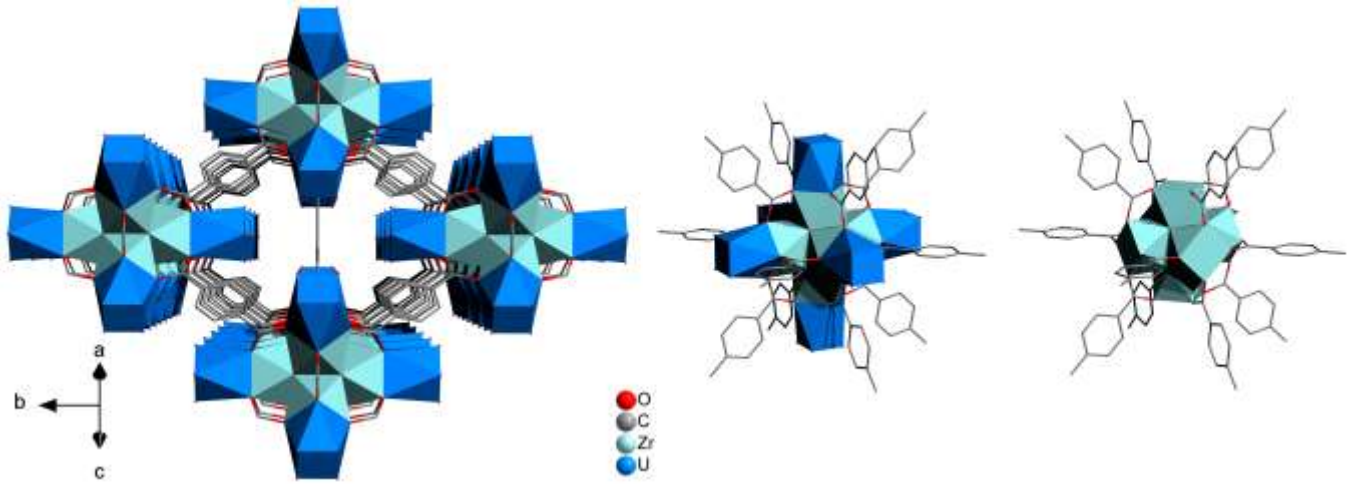

Figure 8 Proposed structure of UiO-66 with bound $[UO_2]^{2+}$ as well as a focused image of proposed binding sites on the Zr_6 node in both their unloaded and loaded forms. Image is intended to show the way $[UO_2]^{2+}$ binds to the Zr_6 node and the overall appearance of a pore of UiO-66 when $[UO_2]^{2+}$ is bound.

UiO-66 U-Zr shell coordination and that of UiO-67 and UiO-67/bpy could be potentially caused by either a distortion in the Zr_6 node from binding or weaker interaction with the Zr, which is evidenced by the higher σ^2 of the U-Zr shell in UiO-66. Overall, these differences in the EXAFS fitting of UiO-66 and UiO-67 as well as UiO-67/bpy do not suggest any difference in the binding site for $[UO_2]^{2+}$ leading to the very similar structure of UiO-66, shown in Figure 8, compared to that of UiO-67 in Figure 7.

Overall Implications Towards Optimizing $[UO_2]^{2+}$ Uptake

The combined results of XRF, XAS, and AWAXS analysis point to certain features that bind and also improve the uptake of $[UO_2]^{2+}$ into Zr MOFs. These findings could be used to further expand upon MOF design for the purposes of $[UO_2]^{2+}$ uptake as well as narrow down the selection of MOFs to be studied in the future. However, through this work alone it can be said that Zr MOFs, and potentially other MOFs as well, will have improved $[UO_2]^{2+}$ uptake when ligands with higher binding affinity for $[UO_2]^{2+}$, in this case porphyrin, are used. Additionally, when the Zr_6 nodes of the MOF have fewer linkers coordinated to them since these sites are viable binding sites for $[UO_2]^{2+}$. Furthermore, the implications of this work extend to a method for evaluating the binding sites of many substances that are incorporated into MOFs, including but not limited to, $[UO_2]^{2+}$. Most notably is the combined use of less well known AWAXS with XAS techniques to correlate and corroborate results between them to provide a conclusion on the structure without the need of crystal structure solution, especially when the uptake of target substances is low and could lead to minimal or unusable changes in diffraction patterns that would make structure solution difficult to impossible as a means to determine binding sites.

Conclusions

In summary, we present a detailed method for the determination of binding sites and uptake of $[UO_2]^{2+}$ via less common X-ray structural analysis techniques and XRF as well as the results of this method on six Zr MOFs. The AWAXS analysis provides identification of crystallographic planes on which $[UO_2]^{2+}$ resides and can be further used to establish potential binding sites. Whereas the XAS analyses provides both information on the electronic structure and local environment of bound U which can be used as a method to corroborate the findings of AWAXS. While XRF provides a means to quantify the uptake of $[UO_2]^{2+}$ it can also be used as a means to further evaluate the accuracy of proposed binding sites and structures. This is because the number of Zr atoms in a unit cell is known from the crystal structure of a MOF. When taking the relative amount of U to Zr, obtained from XRF analysis, the number of bound $[UO_2]^{2+}$ ions in a unit cell can be determined. Therefore, the number of binding sites can be determined as it is directly equivalent to the number of bound $[UO_2]^{2+}$ ions. From this amount of binding sites, the binding sites determined from AWAXS and EXAFS can be evaluated as to whether they meet the necessary number of sites to achieve the uptake seen by XRF. Beyond the method for determining and evaluating binding sites these results provide specific features that improve the uptake of $[UO_2]^{2+}$ and can help narrow down possible MOFs that would be best for the uptake of $[UO_2]^{2+}$, and may be used for remediation, separations, and resource harvesting. While more work will be needed to further narrow down the best MOFs for $[UO_2]^{2+}$ uptake, as well as the reusability of these MOFs for $[UO_2]^{2+}$ uptake. These findings contribute to ongoing work in MOF design and MOF chemistry studies and enable other methods by which to study these materials.

Author Contributions

The project and experimental methods were created by Moreau, Zhang, and Johnson. Synthetic work and XRF data collection was carried out by Johnson. Synthesis, SEM imaging, and nitrogen isotherm of NU-1000 was conducted by Farha and Knapp. SEM imaging of UiO-67 was obtained by Li. XAS data was collected by Bang and Moreau. AWAXS data was collected by Johnson, Moreau, and

Yaw, with assistance from Seifert on AWAXS data collection. AWAXS data was processed by Heaney with assistance from Seifert. XAS data was processed by Bang. XAS and AWAXS data were analyzed and interpreted by Heaney and Moreau. The manuscript was written by Heaney and Moreau and reviewed by all authors.

Conflicts of interest

The authors report no conflicts of interest.

Acknowledgements

This work was supported by the U.S. Department of Energy (DOE), National Nuclear Security Administration (NNSA) under award no. DE-NA0003763. XAS and AWAXS work was performed at the Advanced Photon Source (APS), which is supported by the U.S. DOE, Office of Science under Contract No. DE-AC02-06CH11357. XAS research was conducted at APS beamline 13-ID-E. AWAXS research was conducted at APS beamline 12-ID-C. SEM imaging capabilities were provided by the Franceschi Microscopy & Imaging Center (FMIC) at Washington State University and the Electron Probe Instrumentation Center (EPIC) at Northwestern University. Johnson would like to acknowledge the funding provided by the DOE Office of Nuclear Energy through the Nuclear Energy University Program (NEUP) Fellowship and Washington State supported Research Assistantship for Diverse Scholars (RADS). Heaney would like to acknowledge the funding provided by the Department of Defense (DOD) Army Research Office (ARO) through the National Defense Science and Engineering Graduate (NDSEG) Fellowship. The authors would also like to acknowledge the support provided by the facilitators at the FMIC and EPIC, as well as the Guo Lab at Washington State University for providing access to instrumentation XRF measurements. Lastly, the authors would like to acknowledge the support offered by beamline scientists at the APS and Matt Newville.

Notes and references

1 R. S. Herbst, P. Baron and M. Nilsson, in *Advanced Separation Techniques for Nuclear Fuel Reprocessing and Radioactive Waste Treatment*, eds. K. L. Nash and G. J. Lumetta, Woodhead Publishing, 2011, pp. 141-175.
2 D. Gorman-Lewis, P. C. Burns and J. B. Fein, *J. Chem. Thermodyn.*, 2008, **40**, 335-352.
3 N. A. Smith, G. S. Cerefice and K. R. Czerwinski, *J. Radioanal. Nucl. Ch.*, 2013, **295**, 1553-1560.
4 S. D. Kelly, E. T. Rasbury, S. Chattopadhyay, A. J. Kropf and K. M. Kemner, *Environ. Sci. Technol.*, 2006, **40**, 2262-2268.
5 S. Rout, N. Khandelwal, A. K. Poswal, V. Pulhani and A. V. Kumar, *Environ. Sci-Nano.*, 2021, **8**, 1256-1268.
6 F. Yuan, Y. Cai, S. Yang, Z. Liu, L. Chen, Y. Lang, X. Wang and S. Wang, *J. Radioanal. Nucl. Ch.*, 2017, **311**, 815-831.
7 F. P. Carvalho and J. M. Oliveira, *J. Radioanal. Nucl. Ch.*, 2007, **274**, 167-174.
8 R. E. Norman, 1993.
9 F. P. Carvalho, *Am. J. Environ. Sci.*, 2011, **7**, 547.
10 G. Tian, S. J. Teat, Z. Zhang and L. Rao, *Dalton T.*, 2012, **41**, 11579-11586.
11 C. W. Abney, R. T. Mayes, T. Saito and S. Dai, *Chem. Rev.*, 2017, **117**, 13935-14013.
12 NEA, *Uranium 2020: Resources, Production and Demand*, OECD Publishing, Paris, 2020.
13 D. Mei, L. Liu and B. Yan, *Coordin. Chem. Rev.*, 2023, **475**, 214917.
14 D. Li, H.-Q. Xu, L. Jiao and H.-L. Jiang, *EnergyChem*, 2019, **1**, 100005.
15 A. Karmakar, E. Velasco and J. Li, *Natl. Sci. Rev.*, 2022, **9**, nwac091.
16 S. Dhaka, R. Kumar, A. Deep, M. B. Kurade, S.-W. Ji and B.-H. Jeon, *Coordin. Chem. Rev.*, 2019, **380**, 330-352.
17 S. Pandey, Z. Jia, B. Demaske, O. A. Ejegbavwo, W. Setyawan, C. H. Henager, Jr., N. Shustova and S. R. Phillpot, *J. Phys. Chem. C*, 2019, **123**, 26842-26855.
18 W. Liang, P. M. Bhatt, A. Shkurenko, K. Adil, G. Mouchaham, H. Aggarwal, A. Mallick, A. Jamal, Y. Belmabkhout and M. Eddaoudi, *Chem*, 2019, **5**, 950-963.
19 N. Panagiotou, I. Liatsou, A. Pournara, G. K. Angeli, R. M. Giappa, E. Tylianakis, M. J. Manos, G. E. Froudakis, P. N. Trikalitis, I. Pashalidis and A. J. Tasiopoulos, *J. Mater. Chem. A*, 2020, **8**, 1849-1857.
20 L. L. Song, C. Chen, F. Luo, S. Y. Huang, L. L. Wang and N. Zhang, *J. Radioanal. Nucl. Ch.*, 2016, **310**, 317-327.
21 A. Rajaei, K. Ghani and M. Jafari, *J. Chem. Sci.*, 2021, **133**, 14.
22 X. Qin, W. Yang, Y. Yang, D. Gu, D. Guo and Q. Pan, *Inorg. Chem.*, 2020, **59**, 9857-9865.
23 W. Yang, Q. Pan, S. Song and H. Zhang, *Inorg. Chem. Front.*, 2019, **6**, 1924-1937.
24 S. M. Moosavi, A. Nandy, K. M. Jablonka, D. Ongari, J. P. Janet, P. G. Boyd, Y. Lee, B. Smit and H. J. Kulik, *Nat. Commun.*, 2020, **11**, 4068.
25 L. M. Moreau, A. Herve, M. D. Straub, D. R. Russo, R. J. Abergel, S. Alayoglu, J. Arnold, A. Braun, G. J. P. Deblonde, Y. Liu, T. D. Lohrey, D. T. Olive, Y. Qiao, J. A. Rees, D. K. Shuh, S. J. Teat, C. H. Booth and S. G. Minasian, *Chem. Sci.*, 2020, **11**, 4648-4668.
26 N. Thamavaranukup, H. A. Höppe, L. Ruiz-Gonzalez, P. M. F. J. Costa, J. Sloan, A. Kirkland and M. L. H. Green, *Chem. Commun.*, 2004, 1686-1687.
27 O. N. Batuk, D. V. Szabó, M. A. Denecke, T. Vitova and S. N. Kalmykov, *Radiochim. Acta.*, 2013, **101**, 233-240.
28 U. Schubert, *Coordin. Chem. Rev.*, 2022, **469**, 214686.
29 Z. Lu, J. Liu, X. Zhang, Y. Liao, R. Wang, K. Zhang, J. Lyu, O. K. Farha and J. T. Hupp, *J. Am. Chem. Soc.*, 2020, **142**, 21110-21121.
30 D. Nam, Y. Kim, M. Kim, J. Nam, S. Kim, E. Jin, C. Y. Lee and W. Choe, *Inorg. Chem.*, 2021, **60**, 10249-10256.
31 K. E. Hicks, A. S. Rosen, Z. H. Syed, R. Q. Snurr, O. K. Farha and J. M. Notestein, *ACS Catal.*, 2020, **10**, 14959-14970.
32 N. A. Khan, Z. Hasan and S. H. Jhung, *J. Hazard. Mater.*, 2013, **244-245**, 444-456.
33 M. Hao, Y. Liu, W. Wu, S. Wang, X. Yang, Z. Chen, Z. Tang, Q. Huang, S. Wang, H. Yang and X. Wang, *EnergyChem*, 2023, 100101.
34 H. Li, F. Zhai, D. Gui, X. Wang, C. Wu, D. Zhang, X. Dai, H. Deng, X. Su, J. Diwu, Z. Lin, Z. Chai and S. Wang, *Appl. Catal. B-Envrion.*, 2019, **254**, 47-54.
35 T. G. Semerci, A. Melillo, Y. Ç. Mutlu and H. Garcia, *Catal. Today*, 2023, **423**, 113931.
36 S. L. Hanna, D. X. Rademacher, D. J. Hanson, T. Islamoglu, A. K. Olszewski, T. M. Nenoff and O. K. Farha, *Ind. Eng. Chem. Res.*, 2020, **59**, 7520-7526.
37 Ş. Tokalıoğlu, E. Yavuz, S. Demir and Ş. Patat, *Food Chem.*, 2017, **237**, 707-715.
38 A. Amini, M. Khajeh, A. R. Oveisi, S. Daliran, M. Ghaffari-Moghaddam and H. S. Delarami, *Ind. Eng. Chem. Res.*, 2021, **93**, 322-332.

39 M. J. Katz, Z. J. Brown, Y. J. Colón, P. W. Siu, K. A. Scheidt, R. Q. Snurr, J. T. Hupp and O. K. Farha, *Chem. Commun.*, 2013, **49**, 9449-9451.
40 T. Islamoglu, K.-i. Otake, P. Li, C. T. Buru, A. W. Peters, I. Akpinar, S. J. Garibay and O. K. Farha, *CrystEngComm*, 2018, **20**, 5913-5918.
41 W. Morris, B. Volosskiy, S. Demir, F. Gándara, P. L. McGrier, H. Furukawa, D. Cascio, J. F. Stoddart and O. M. Yaghi, *Inorg. Chem.*, 2012, **51**, 6443-6445.
42 J. B. DeCoste, G. W. Peterson, H. Jasuja, T. G. Glover, Y.-g. Huang and K. S. Walton, *J. Mater. Chem. A*, 2013, **1**, 5642-5650.
43 C. Koschnick, R. Stäglich, T. Scholz, M. W. Terban, A. von Mankowski, G. Savasci, F. Binder, A. Schökel, M. Etter, J. Nuss, R. Siegel, L. S. Germann, C. Ochsenfeld, R. E. Dinnebier, J. Senker and B. V. Lotsch, *Nat. Commun.*, 2021, **12**, 3099.
44 B. Ravel and M. Newville, *J. Synchrotron Radiat.*, 2005, **12**, 537-541.
45 A. L. Ankudinov, B. Ravel, J. J. Rehr and S. D. Conradson, *Phys. Rev. B*, 1998, **58**, 7565-7576.
46 J. Ilavsky, *J. Appl. Crystallogr.*, 2012, **45**, 324-328.
47 J. Ilavsky and P. R. Jemian, *J. Appl. Crystallogr.*, 2009, **42**, 347-353.
48 B. H. Toby and R. B. Von Dreele, *J. Appl. Crystallogr.*, 2013, **46**, 544-549.
49 I. Goodenough, V. S. D. Devulapalli, W. Xu, M. C. Boyanich, T.-Y. Luo, M. De Souza, M. Richard, N. L. Rosi and E. Borguet, *Chem. Mater.*, 2021, **33**, 910-920.
50 D. Feng, W.-C. Chung, Z. Wei, Z.-Y. Gu, H.-L. Jiang, Y.-P. Chen, D. J. Darensbourg and H.-C. Zhou, *J. Am. Chem. Soc.*, 2013, **135**, 17105-17110.
51 J. G. Knapp, X. Zhang, T. Elkin, L. E. Wolfsberg, S. L. Hanna, F. A. Son, B. L. Scott and O. K. Farha, *CrystEngComm*, 2020, **22**, 2097-2102.